Bottom time spread and bistatic scattering by rough basalt

Ronald L. Dicus

Science Applications International Corporation, 1710 Goodridge Drive
McLean, Virginia 22102.

Abstract: Scattering from oceanic basalt affects low-frequency active sonar systems in at least two important ways: (1) Significant time, angle and frequency spreading reduces target echo levels when systems over-resolve the spread; (2) Scattering causes significant reverberation. This paper examines time spreading and bistatic reverberation in an environment where rough basalt dominates. Both measurements and model predictions will be discussed.

Measurements were made on an array of 64 elements with 1/2 wavelength spacing at 160 Hz, towed at a depth of 200 m. Mk-61 SUS charges were deployed at 244 m depth in water 5000 m deep. The site was in a thin-sedimented, rough-bottom, abyssal-hill province of the Northeast Pacific. Scattering in this environment presents a continuous diffuse return (no coherent component).

To investigate bottom time spreading effects, the magnitude-squared envelope of the bottom pulse response was analyzed for a single omni hydrophone. Comparisons were made within frequency bands from 100 Hz to 300 Hz and over grazing angles from 80° to 10°. Theoretical predictions were generated using Kirchhoff theory in the high-frequency limit with two different slope density functions: (1) the measured slope density function derived from Seabeam bathymetry at the measurement site, and (2) a slope density function taken from Deep Tow bathymetry, not at the measurement site but instead at the crest of the East Pacific Rise. The Seabeam slope density function was unable to explain the long-duration, low-level tail of the acoustic time spread functions. However, the high-resolution Deep-Tow-derived slope density function gave excellent predictions. The theoretical model appears to offer a satisfactory explanation of the observed time spread functions including their absolute levels. The effect on system loss was computed as a function of bandwidth. The computation showed that large-bandwidth systems may suffer significant additional signal losses.

Bistatic scattering was also examined by comparing predicted and measured beam power time series. Bistatic scattering strength was computed from the model as a function of bistatic angle for given source and receiver grazing angles. Scattering strengths were generally larger than Lambert's law and significant bistatic angle dependence was demonstrated.

1. Introduction

The Pacific abyssal hills are characterized as elongated hills a few hundred meters high, a few kilometers wide, and perhaps 10's of kilometers long. The pelagic sediments accumulate to less than 75 m depth and overlie rough oceanic basalt. Thin sediment overlying oceanic basalt is also found immediately adjacent to many shallow-water, narrow-shelf, coastal waters including the Tyrrhenian Sea, West Arabian Sea, and Pacific Rim. The Pacific Rim includes the Aleutians, Japan, Taiwan, Philippines, Indonesia,

Coral Islands, and New Zealand. Associated back arc basins include parts of the Kuril basin, Sea of Japan, Philippine Sea, South China Sea, Coral Sea, and Tasman Sea.

The acoustic pulse response from the basalt interface is characterized by a long, slowly decaying tail with durations on the order of 1 sec. McCammon [1] has modeled time and angle spreads for this type of environment by assuming a Gaussian slope density function and fitting the data with a 2.5° to 3° surficial RMS slope on a 5 m thick, sediment layer and a 20° RMS slope for the basalt basement. The 2-dimensional RMS slope of 20° corresponds to a 1-dimensional RMS slope of 14°. The model accounts for the top 10 to 20 dB of the pulse response but fails to predict the remaining slowly decaying tail. High resolution bathymetric data [2,3] shows a non-Gaussian slope density function. We will see that the non-Gaussian function predicts the complete time spread observed and requires no roughness scattering from the water-sediment interface.

This paper offers an explanation for the long time spreads based on Kirchhoff scattering theory and a slope density function taken from Deep Tow measurements. It will be shown that incorporation of this function together with the reflectivity function for an elastic half space with basaltic properties leads to predicted time series in good agreement with measurements. In particular, the theoretical time spread function for omni-directional source and receiver exhibits the long time-spread tail and recreates the absolute levels with no adjustable parameters. The large time spreads have implications for large bandwidth systems. It will be shown that the effective bottom loss for a system increases significantly with bandwidth. In addition, the same model predicts the associated bistatic scattering strengths. The scattering strengths are found to be generally larger than Lambert's law and to have a significant dependence on bistatic angle.

2. Experiment

The term "Pacific Echo" refers to a series of experiments in the Pacific conducted jointly by the Naval Research Laboratory, Washington DC and Defence Research Establishment Pacific, Victoria BC. The first experiment (Echo I) occurred in June of 1986 using US DESTEIGUER as the source ship for deploying Signal Underwater Sound (SUS) charges, and CFAV ENDEAVOUR as the receiver ship for towing the receiving array. The second experiment (Echo II) followed in October of 1988. The experimental geometry is shown in Fig. 1. The receiver ship towed the array at 200m depth and 4 kts speed while the source ship executed an opening track from a range of 0.5 km to 40 km while deploying MK-61 SUS at a depth of 244m.

The horizontal array consisted of a VLF aperture of 32 elements equally spaced 37.5m apart (design frequency = 20 Hz) and a high frequency aperture of 64 elements equally space 4.7 m apart (design frequency = 160 Hz). Hydrophone elements consisted of groups of 10 hydrophones each. The grouping helps attenuate flow noise. A diagram of the array is shown in Fig. 2. Only one of the omni-directional hydrophones was used for this analysis of time spread. Environmental measurements included eXpendable Sound

Velocity (XSV) profiles from the receiver ship, eXpendable BathyThermograph (XBT) profiles from the source ship, and 3.5 kHz depth profiles from the source ship. Data analyzed in this report is from the second experiment at a station located at 34°04'N, 138°20'W.

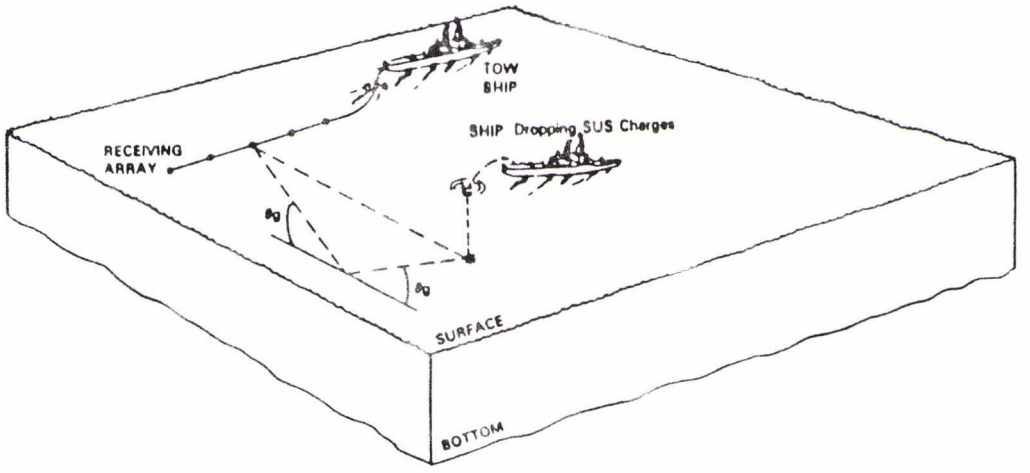

Fig. 1. Experiment configuration.

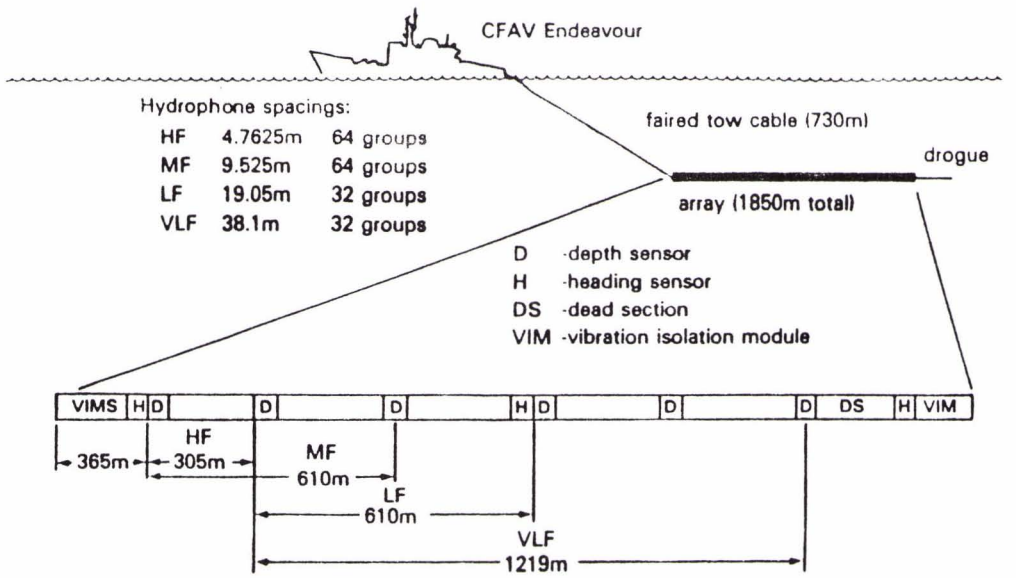

Fig. 2. Diagram of towed array.

The array was towed in an east-west direction at 4 kts. The source ship started the run a short distance from the center of the array and steamed at 6 kts on a bearing 65° relative to the array track. The geometry placed the source at a fixed bearing of 15° relative to broadside. The advantage of this asymmetrical geometry is that the source stays out of the broadside beam where occasionally under very low signal conditions common-mode-type electronic noise may dominate.

In May of 1989 the Scripps Institute of Oceanography collected Seabeam measurements along the east-west track of Pacific Echo II. Seabeam is a high resolution multi-beam swath mapping bathymetric system. The output is bottom topography (bottom depth) over a swath approximately 4.5 km wide at the depth of 5 km. In addition a water gun was towed emitting pulses (without bubble pulses) that penetrated the water-sediment interface and reflected off the underlying basalt. The difference between the two depths gives sediment thickness, which averaged 25 m along the track.

3. Model

The model implementation developed to interpret this data is new, but the model itself is not. Classical scattering theory is invoked in the form of the Kirchhoff or tangent-plane approximation in the high frequency limit. The tangent plane approximation is appropriate for large-scale scattering--scattering from roughness features whose deviations from the basal plane are large compared to a wavelength and yet sufficiently smooth. Large roughness means the Rayleigh parameter is much greater than unity, i.e.

$$k\sigma \sin\psi >> 1$$

where k is acoustic wavenumber, σ is the RMS surface deviation, and ψ is the grazing angle. The smoothness requirement may be quantified by a constraint on the radius of curvature and grazing angle of incidence as expressed by the following inequality:

$$\sin\psi >> (ka)^{-1/3}$$

where $k = 2\pi/\lambda$ is the acoustic wavenumber, λ is the acoustic wavelength, and a is the surface radius of curvature. That large scale scattering approximations are appropriate for this data set is clear from observation of typical bathymetric time series or by computation of an RMS height measure. In this case the RMS height is on the order of 40 m, which is much larger than a wavelength for frequencies up to the 300 Hz limit of this data set.

Shadowing and multiple scattering are ignored. This is reasonable as long as grazing angles are larger than the mean square bottom slope. The source and receiver are assumed to be in the far field, i.e.

$$kS >> 1$$

where S is the slant range from source or receiver (S_s or S_r) to a scattering point on the rough surface. The mean square height must be much less than a Fresnel zone radius, i.e.

$$(k\sigma^2 \sin^2\psi) / S << 1$$

The high-frequency limit requires that

$$(q_z\sigma)^2 >> 1, \quad if \frac{q_\perp}{q_z\gamma} \leq 1$$

$$(q_z\sigma)^2 >> \left(\frac{q_\perp}{q_z\gamma}\right)^4, \quad if \frac{q_\perp}{q_z\gamma} \geq 1$$

where γ is the RMS slope, and q_p and q_z are the perpendicular component (projection onto the basal plane) and z-component, respectively, of the vector $\vec{q}$, where

$$\vec{q} = \vec{\kappa} - \vec{k}$$

and $\vec{\kappa}$, $\vec{k}$ are the vector wavenumbers in the direction of the outgoing scattered wave and incoming plane wave, respectively.

The solution for the scattered field may then be written in differential form

$$dr_s = |V(\theta)|^2 (q/q_z)^4 p_\gamma(-q_\perp/q_z) dA/(4S_s^2 S_r^2)$$

where dr_s is the differential scattered field at the receiver, p_γ is the probability density function for bottom slope, dA is the differential area, and $|V(\theta)|$ is the plane-wave amplitude reflection coefficient.

The intensity response for an impulsive source signal of unit energy is found by replacing dA in the above equation with dA/dt and integrating along the elliptic contour of equal travel time. The term dA in this context is a differential element of area at a point on the contour in the differential annulus formed between the two ellipses associated with time t and t+dt, respectively. The time series arises from bottom scatterers illuminated by the expanding travel time ellipse. The full ellipse corresponds to the omni receiver case. For a directional receiver the ellipse is overlaid by the receiver beam pattern. For the calculations presented here a simplification was made. The beam pattern for the array was assumed to be an ideal sector (bounded by straight lines) of width equal to the Hann shaded main-lobe beamwidth at the -3 dB points. Sidelobe energy was neglected. More precisely, the beam pattern for a horizontal array intersects the bottom in a family of hyperbolas (not straight lines). Intersection of a hyperbola and an ellipse defines the scattering patch. However, the simpler idealized beam pattern assumed here was found to give good results.

For the reflection coefficient in the above equation for scattering strength the plane wave reflection coefficient for water overlying a basaltic half space was used. The plane wave reflection coefficient is calculated at a grazing angle that depends on the location of the differential scattering patch. The angle is equal to the grazing angle that the incident ray makes with a specular facet at that bottom location. A specular facet is one oriented for specular reflection between source and receiver at the location of the scatterer. The basalt parameters used for the reflection coefficient calculation are as follows:

Density, ρ=2.5
Compressional wave speed, c_l=5 km/sec
Shear wave speed, c_t=2.5 km/sec

This result and accompanying assumptions above follows the development of Bass and Fuks [4]. By far the most important component in this recipe is the slope density function. The slope density function and its non-Gaussian long tails are responsible for the large time spreads and associated angle and Doppler spreads typically observed in Pacific thin sediment areas.

Past work often assumed a Gaussian slope density function because of analytic simplicity and because, in many stochastic phenomena, non-Gaussianity leads to minor second order effects. Indeed, if one plots the slope density function used here along with the Gaussian function of the same RMS slope on *linear* axes of probability versus slope, the non-Gaussian deviation appears to be of minor importance, hence the temptation to ignore it because we are still trying to explain major first-order effects.

The importance of the non-Gaussian tail is more easily appreciated if the density functions are plotted on semilog graph paper (a fair representation because the time-spread reverberation from the scattered field interferes with target detection in accordance with the ratio of scattering intensities). This brings into perspective the behavior at low probability levels. The shape of the Gaussian is concave downwards at first and drops precipitously below the non-Gaussian curve. Meanwhile the non-Gaussian curve is virtually a straight line, i.e. exponential in fall-off, over the entire range. This difference in fall-off rates is obscured in the linear plots.

Because the fall-off rate of the measured slope-density function is so much slower than the Gaussian curve, the energy associated with these low levels can still be significant because of the long integration times involved. A second feature which we will see in the acoustic predictions is that the geometric mapping of the slope density function into time is highly nonlinear and the straight line behavior near zero slope actually gets mapped into a very peaked acoustic response in time. Thus, a very sharp peak is predicted in the incoherent scattered field which is not the same as the coherent reflection produced by the mean smooth plane.

3.1 Slope density functions.

Slope density functions may be numerically estimated from high-resolution bathymetric data. For the purposes of scattering theory, surface slope is the two-dimensional surface-height-gradient vector, which lies in the basal plane of the rough surface. In the simplest case azimuthal isotropy is assumed; then, all bathymetric lines are realizations from the same population of surface heights. Bathymetric time series may be differenced to obtain a time series of slopes projected onto an axis (x-axis) coincident with the bathymetric line. The ensemble of these slope projections forms a marginal distribution since the orthogonal projection (y-component) is also being randomly sampled. That is, the one-dimensional distribution of slopes obtained from measurements along the x-axis is an estimate of the two-dimensional slope distribution integrated over the y-component of slope.

For the isotropic function, appeal is made to a very powerful theorem [5] that states that a probability density may not be simultaneously non-Gaussian and isotropic with independent marginal densities. We must refrain from creating a two-dimensional density simply as the product of the x and y, one-dimensional marginal densities. The isotropic density is circular symmetric, and the relationship between one- and two-dimensional densities in the case of circular symmetry is contained in the theory of Abel transforms [6]. The inverse Abel transform provides the means for obtaining the radial density of the two-dimensional density from the one-dimensional marginal density.

Consider the two-dimensional slope density function, $p_2(\gamma_x, \gamma_y)$. A one-dimensional slope density function may be constructed from a histogram of slopes derived from the marginal differencing of an equi-spaced bathymetric time series taken along say the x-axis. Each frequency-of-occurrence bin is filled with members having the same x-component of slope but with randomly occurring y-component slopes. The resulting probability density is an estimate of the marginal density defined by

$$p_1(\gamma_x) = \int_{-\infty}^{\infty} p_2(\gamma_x, \gamma_y) d\gamma_y = 2\int_0^{\infty} p_2(\gamma_x, \gamma_y) d\gamma_y .$$

If we assume circular symmetry, then

$$p_2(\gamma_x, \gamma_y) = p(\gamma_r)$$

where,

$$\gamma_r^2 = \gamma_x^2 + \gamma_y^2 .$$

Substituting for γ_y and $d\gamma_y$ we arrive at

$$p_1(\gamma_x) = 2\int_{\gamma_x}^{\infty} \frac{p(\gamma_r)\gamma_r d\gamma_r}{(\gamma_r^2 - \gamma_x^2)^{1/2}} .$$

This expression for $p_1(\gamma_x)$ is identical to the Abel transform [6] of $p(\gamma_r)$. We can obtain the radial density from the x-component marginal density by inverting via the definition of the inverse Abel transform. From reference [6] the result is

$$p(\gamma_r) = -\frac{1}{\pi}\int_{r}^{\infty} \frac{p_1'(\gamma_x) d\gamma_x}{(\gamma_x^2 - \gamma_r^2)^{1/2}} .$$

The slope density function proposed in this modeling effort is taken from the Deep Tow measurements and slope distribution analysis of Larson et al. [2] and Spiess et al. [3]. These authors compiled the statistics on the occurrence of bottom facet slopes. Their instrumentation consisted of 40 kHz echo sounders (beamwidth = 4°) towed from 50 m to 500 m off the bottom. Sub-bottom information was obtained with a 3.5 kHz source. No beamwidth was specified for this source except for the statement that the beam was broader and more powerful than the 40 kHz echo sounders. The sounding data was sampled from analog records at distances such that straight line segments nowhere departed more than 2 m from the observed trace. Each such segment provided a sample of bottom slope (This author expects that such processing adds white noise of RMS amplitude 2 m to the bathymetric time series). Larson and Spiess present the data in a

histogram of segment sizes that shows a minimum value of 100 m. This suggests that the effective lateral resolution of the measurement is on the order of 100 m.

Larson and Spiess analyzed measurements taken in an area 5 km x 20 km at the crest of the East Pacific Rise (20°54'N,109°13'W) and at another site on the western flank (32°25'N, 125°40'W). They discriminated between tracks along the strike and across the strike of the ridge axis. Slopes were higher across the strike. Similarly, they discriminated between the water-sediment interface and the basalt interface. As might be expected slopes from the basalt interface were higher. Presumably the ponding of sediments reduces some of the larger slopes in favor of the zero slopes for the flat top sediment ponds.

For the modeling presented here the distribution for the basalt interface was used. Differences between across strike and along strike distributions were noted by Larson and Spiess; however, based on the model, these differences are expected to result in less than 1 dB difference in acoustic level at long time spreads. Hence, a two-dimensional isotropic density function was derived from the across strike basement distribution. The one-dimensional density provided by Larson and Spiess and the extrapolation to higher slopes is shown in Fig. 3. A comparison of the two-dimensional slope density functions for the Gaussian, Seabeam, and Deep Tow cases is shown in Fig. 4.

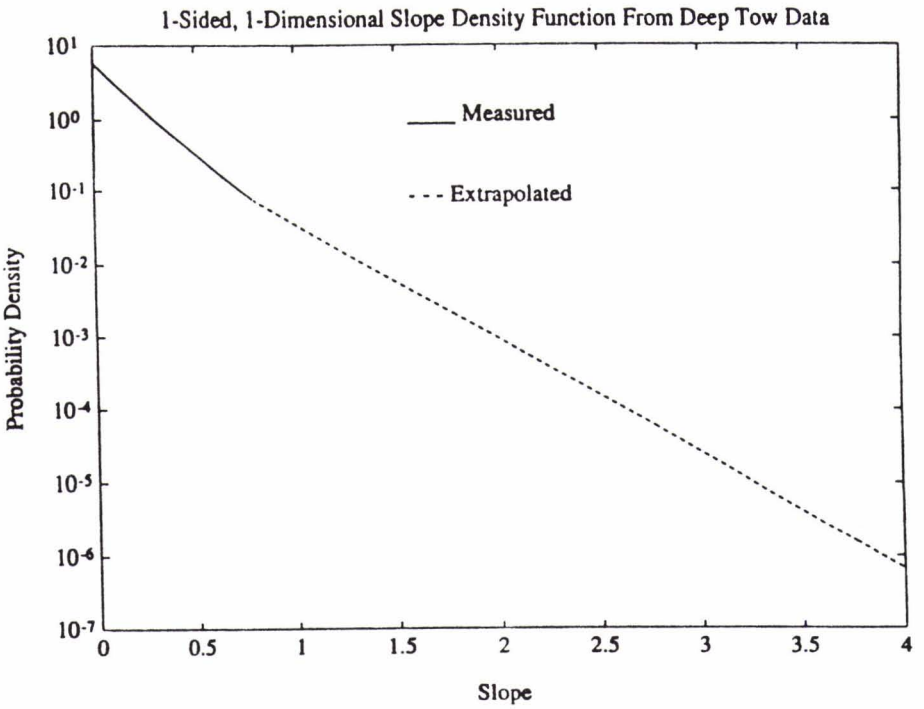

Fig. 3. 1-dimensional slope density function from Deep Tow data showing measured and extrapolated parts.

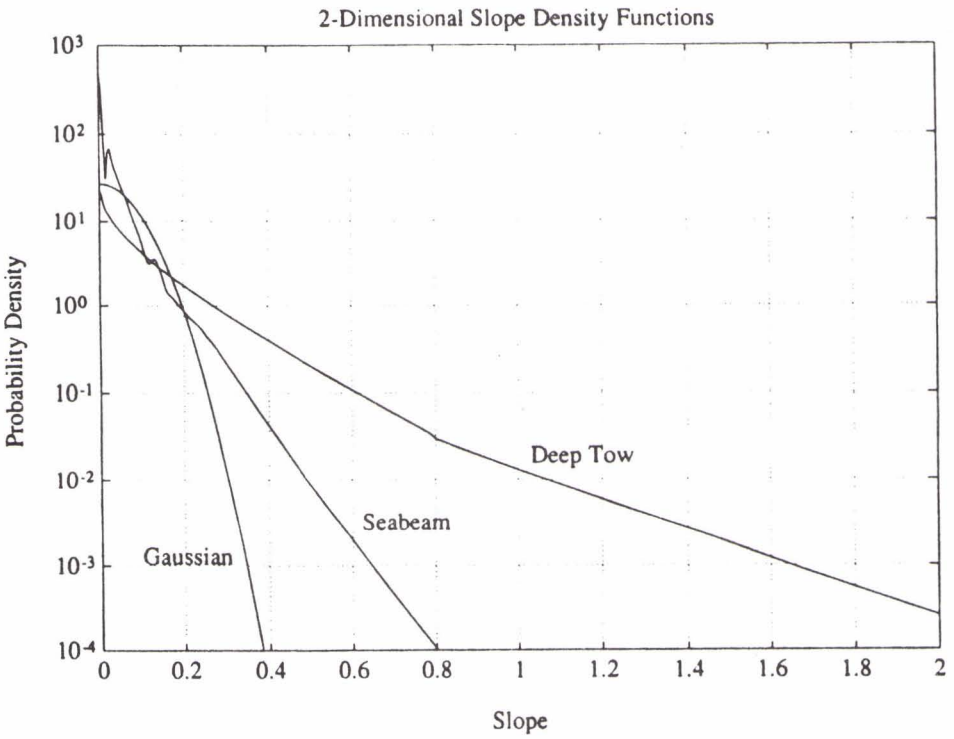

Fig. 4. 2-dimensional slope density functions for the Gaussian, Seabeam, and Deep Tow cases.

4. Results

4.1. Time Spread

To illustrate the performance of the above model several bottom reflected time series are compared with theoretical predictions. The time series were taken from a single omni-directional hydrophone and filtered in a band from 100 Hz to 300 Hz using a three-section Chebyshev digital filter. Amplitudes were corrected for system transfer function and topside amplifier gains. A ray trace program was run to calculate transmission loss along the bottom reflecting path. Correction was made in received levels to remove transmission loss, source level, and bandwidth. The filtered amplitudes were squared and the resulting intensity series smoothed with a three-section low-pass filter with an effective integration time of .05 s. This gave 10 degrees of freedom to the statistical estimates with minimum distortion even at the beginning of the response where the fall-off rate is very rapid.

Three theoretical predictions were generated for comparison. The first was the Gaussian model. The Gaussian model needs only one parameter, the RMS slope. The RMS slope was computed from Seabeam data taken along the acoustic track. The second model used a slope density function derived from the Seabeam data. Sensitivity of the slope density function to sample length and location of the bathymetric series was examined qualitatively and found to be unimportant. The third model used the Larson and Spiess slope density function derived from Deep Tow data.

Figure 5 shows the comparison of the three models at a bottom grazing angle of 79.5°. Because the data contained contributions from all four surface multiples for a single bottom interaction the theoretical time series were generated by adding the predicted intensity time series 4 times with appropriate time delays.

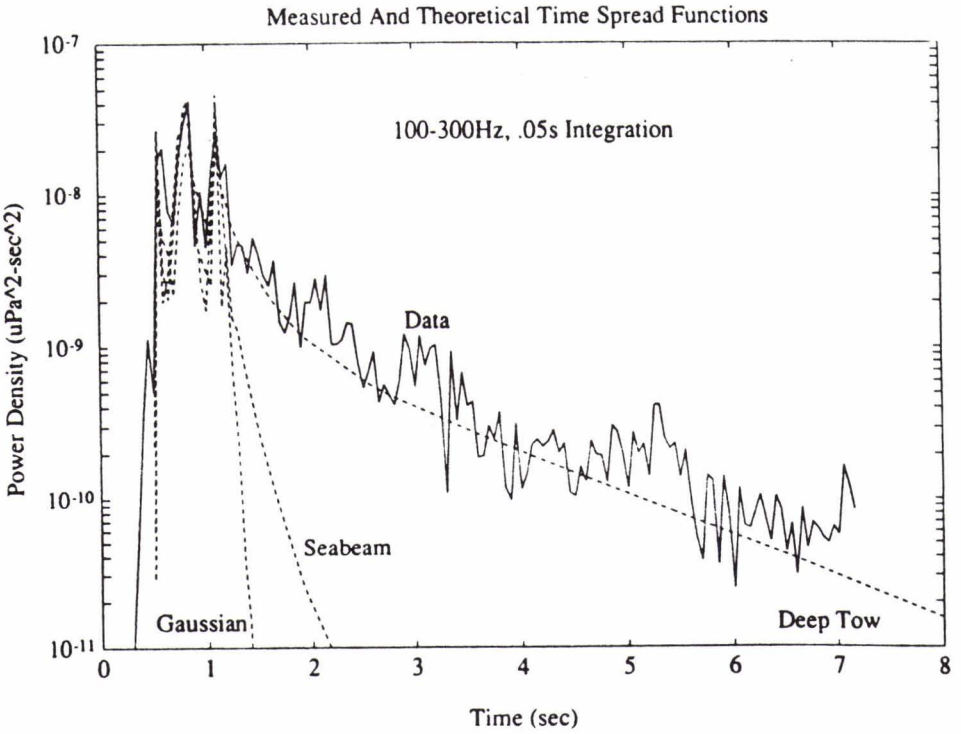

Fig. 5. Measured and theoretical omni time spread functions; grazing angle = 79.5°.

While all three models are in good agreement in the first 0.2 sec of each multiple peak, a dramatic difference is noted at long time delays. Only the Deep-tow-derived slope density function provides an adequate prediction. The prediction is good over the 6.5 sec of available first bounce data representing nearly 30 dB of dynamic range. The basalt parameters chosen are typical of laboratory measurements for dredged basalt samples. The model assumes no sediment effects such as refraction, i.e. just the rough basalt interface is assumed.

Figure 6 shows the data theory comparison for a grazing angle of 22°. The ordinate of this plot, which is different from that of Fig. 5, is a normalized power density. The normalization gives the power in the 100 Hz to 300 Hz band expressed as a per Hz power density, for an impulsive source of unit energy corrected to a transmission loss of 0 dB. This isolates the time spread function from the source and transmission loss terms in the sonar equation. The integral over all time then gives the total energy bottom loss.

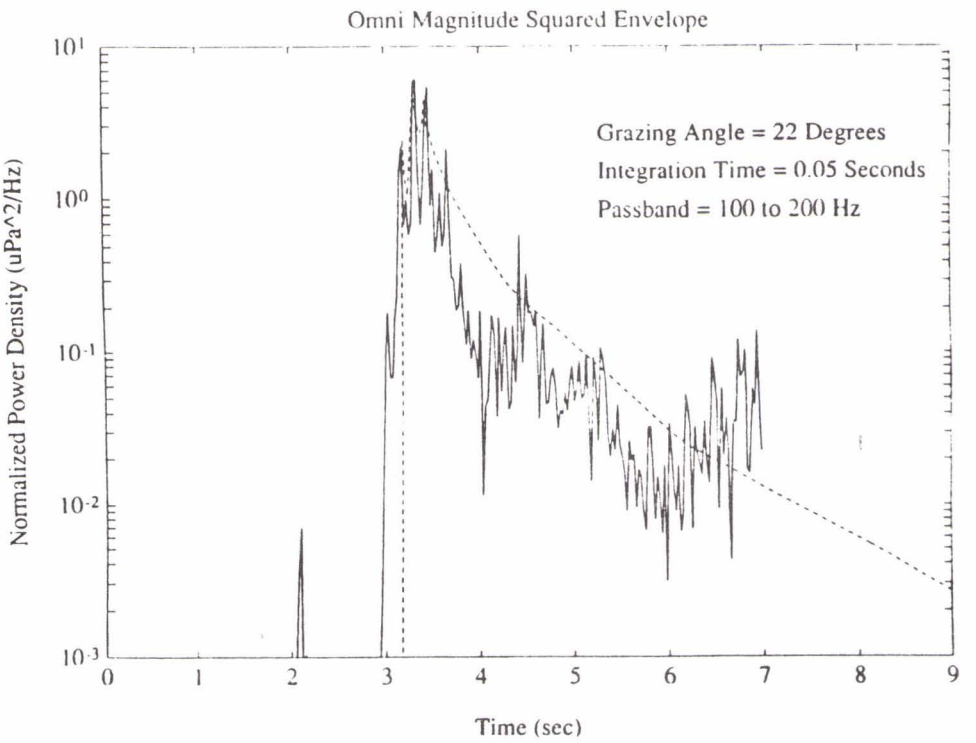

Fig. 6. Measured and theoretical omni time spread functions; grazing angle = 22°.

Because the magnitude-squared envelope has initial sharp peaks followed by a long, slowly decaying tail, the response of systems with different bandwidths will be different. For a bottom impulse-response that decorrelates rapidly compared to the decay of its envelope, the system power response may be calculated by the convolution of the square of the source signal with the mean magnitude-squared envelope. The magnitude-squared-envelope response of the bottom is measured with a pulse that is short relative to time over which the envelope changes significantly. Convolutions were calculated for sinusoidal pulses of various pulse lengths. Fig. 7 shows the results with inverse pulse length expressed as bandwidth. After convolution the peak power divided by the source peak power is shown as peak bottom loss. Similarly, the ratio of total energies is shown as total energy bottom loss. The results at high and low grazing angles are also shown. We see that because of the large time spreads significant additional effective bottom losses are sustained by large bandwidth systems.

An example of the array beam response is shown in Fig. 8. The source-receiver range for this shot produced a nominal grazing angle of 46.5°. The bearing of the source was 107.5° and the beam was steered towards the source. Sharp multipath spikes can be easily discerned. The first such spike in the data is anomalously low, but the other two spikes are on the order of 1 dB lower than the model. The rest of the decay shows a lot of fluctuation as usual but the mean response is well represented by the model.

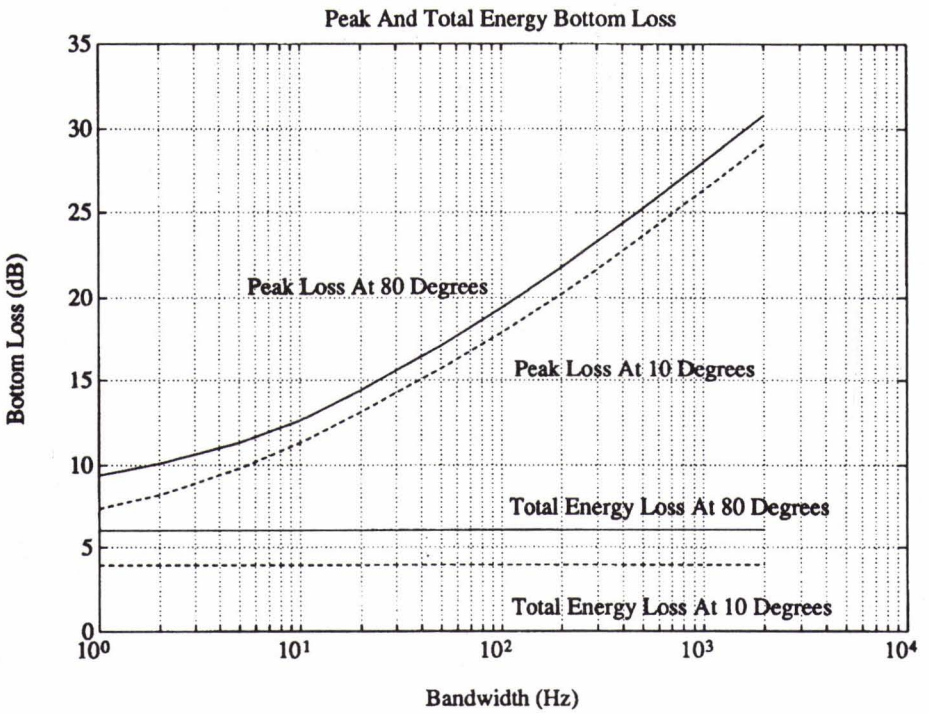

Fig. 7. Peak- and total-energy bottom loss versus bandwidth.

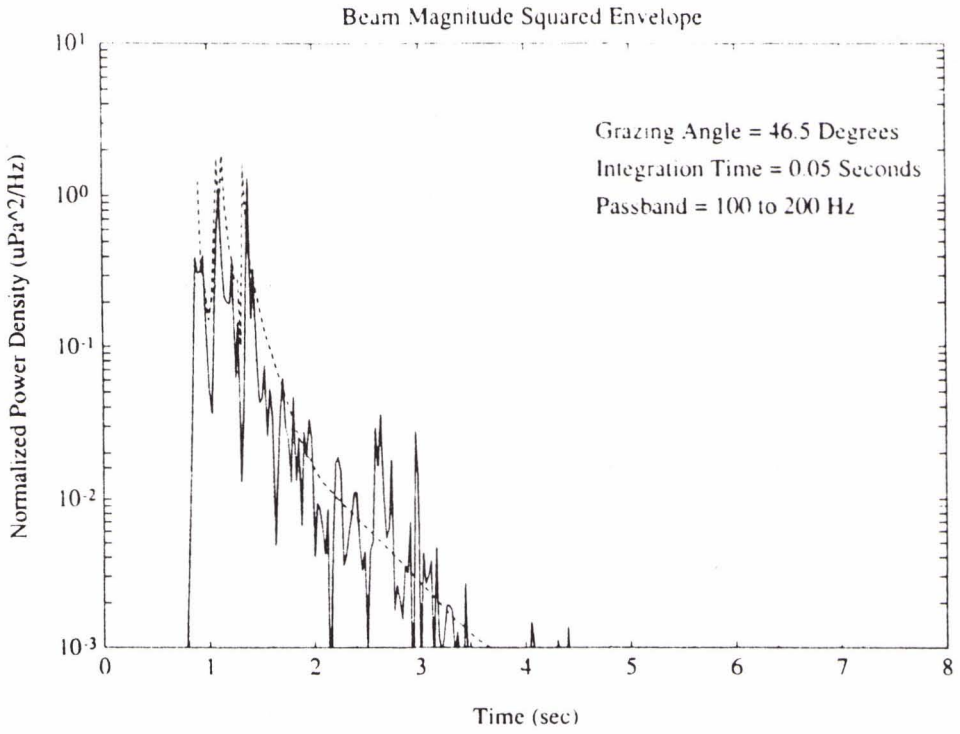

Fig. 8. Measured and theoretical beam time spread functions; grazing angle = 46.5°.

4.2. Bistatic Scattering Strength

Modern warfare scenarios increasingly employ multiple platforms to perform mine hunting and anti-submarine warfare tasks. Active sonars transmit pulses that are not only returned to the transmitting platform but are also received on other platforms. When propagating paths include the bottom, reverberation is received via available bottom scattering patches and the reverberation is termed bistatic reverberation. Obviously, prediction of bistatic reverberation is as important to multistatic operations as monostatic reverberation is to single platform operations. Yet, insufficient attention has been paid to the bistatic aspects of reverberation.

The term scattering strength has long been associated with backscattering, i.e. scattering back to the source. In a monostatic configuration, in which the source and receiver are collocated, all scattering is backscattering and the interaction is specified in terms of a single angle, the grazing angle between the incident beam of energy and the scattering plane. A bistatic configuration, in which source and receiver are spatially separated,

involves three angles for any scattering patch: the grazing angle from the source, the grazing angle to the receiver, and the bistatic angle. The bistatic angle is the angle between the projections onto the scattering plane of the vectors connecting source and receiver to the scattering patch. We will adopt the convention that 0° is in the forward direction and that 180° is in the direction back towards the source.

A scattering-strength model is at the heart of any reverberation prediction. Lambert's law is often employed as the scattering-strength kernel because it often gives an approximate prediction. However, measured scattering strengths often differ markedly from Lambert's law. When it does we often have no knowledge as to why. When it is known that the scattering law for a given area is different from Lambert's law, it is important to the fidelity of reverberation prediction to implement the correct scattering strength function.

We shall see that oceanic basalt is just such a case in which the scattering strength is not represented by the cosine dependence on incoming and outgoing grazing angles. Furthermore, a strong bistatic angle dependence is seen that is totally absent from Lambert's law.

Bistatic scattering strength modeling is a natural outgrowth of time-spread studies. After all, the physical mechanisms are the same regardless of whether their effects appear at different places within the sonar equation. In the case of basalt scattering the return is all incoherent scattering. Hence, there is really no distinction between what we would call signal-path or target-path energy (that occurs close to the first arrival along the specular path) and all other energy that keeps pouring in from increasingly farther scattering sites. There is no time demarcation in the received time series or Fresnel zone on the bottom that separates signal energy from reverberation. We will simply look at the totality of received energy in two different ways. For signal considerations we want to know what effective bottom loss accounts for losses of signal energy for a given processor. For reverberation we want to know how to describe the angular dependence of scattered energy.

From the theory the relationship between the calculated received field and scattering strength is straightforward. The scattering strength (SS) is simply the received intensity per unit scattering area at unit distance from the scatterer in an incident field of unit intensity. For the model discussed here SS is simply written:

$$SS = |V(\theta)|^2 \left(q/q_z\right)^4 p_\gamma\left(-q_\perp/q_z\right)/4$$

where all quantities are as previously discussed.

As with the beam time series the location of scattering patches contributing at a given instant in time is determined in our simplified model by the intersection of the travel time ellipse and the azimuthal rays approximating the main lobe in the array beam pattern for a particular steering direction. In general the rays for the steered beam and the symmetric conjugate beam can intersect the ellipse in 0 to 4 different places. When there is a single intersection, and in the limit of a very narrow beam, the beam ray is tangent to the ellipse. In this case main beam energy has been scattered from a single spot on the bottom. In

effect, it constitutes a direct measurement of bistatic scattering strength at some angle of interaction. At later times more than one intersection occurs and the received main-lobe energy is a result of scattering from at least two different sets of interaction angles.

An example is shown in Fig. 9 of the evolution of the interaction angles with time. This example corresponds to the beam time series displayed in Fig. 8. The angle Phi is the bistatic angle, Chi is the grazing angle to the receiver and Psi is the grazing angle from the source. The different solutions are indicated by the solid and dashed lines. Time is measured relative to the travel time along the specular path.

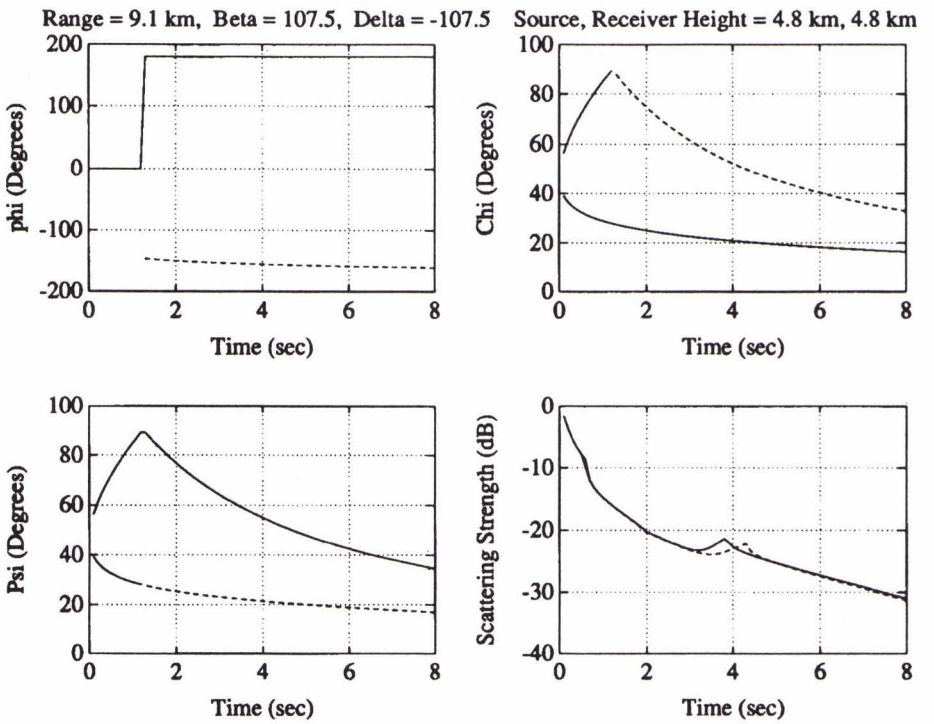

Fig. 9. Interaction angles and scattering strength versus time. Grazing angle of the mean surface specular point = 46.5°. The angle Phi is the bistatic angle, Chi is the grazing angle from scattering patch to receiver, and Psi is the grazing angle from source to scattering patch. Delta is the angle between the endfire direction of the array and the line connecting source and receiver, and beta is the steered angle relative to endfire.

At just after one second in the plots of Phi, Chi, and Psi a change of solution is shown. Since the source and receiver are at nearly the same depth in this calculation the solution changes when the scattering point moves directly under the source for one path and directly under the center of the array for the other path. Notice that because the source is slightly off of broadside the symmetry is broken so that Phi is exactly 180° for the beam pointing to the source but the conjugate beam is not along the line joining source and receiver. As a result Phi for the second solution differs a little from -180°. The asymmetry is not nearly as evident in the curves for Psi and Chi.

The scattering-strength curve is one of the most interesting. In addition to the general trend with time a depression is seen which corresponds to an interval in which the basalt reflectivity is between the compressional and shear critical angles. At a little less than four seconds the compressional critical angle is reached, and near one-half second the shear critical angle is attained. The reduction in basalt reflectivity becomes expressed in the interval of reduced scattering strength..

Calculations at shorter arrival times than shown in Fig. 9 indicate that the first arrival occurs at a grazing angle of 47°. Specification of the scattering strength at short times brings up a bandwidth issue because the scattering strength continues to rise rapidly with decreasing time. Specifically, at t=.001 sec the scattering strength is 5.2 dB and at .0001 sec it is 7 dB. What is being described here is the sharp scattering-strength peak in the vicinity of the specular direction. The implication is that a large bandwidth system is needed to measure the full extent of the scattering strength peak in the specular direction.

At directions away from specular the problem goes away. Thus, we may choose the time series from a beam that misses the specular point. The first arrival still comes from a single scattering patch, but the decay with time is not as rapid. Examination of several beam time series in this way showed that first arrival peaks fluctuated above and below (on the order of 3 dB) the model predictions from beam to beam. This suggests a manifestation of fluctuations rather than a deterministic departure of scattering strength behavior from the model. Furthermore, the omni time series which are predicted well by the model, are really the result of scatterers from many beams which helps to average out such beam-to-beam fluctuations.

Therefore, we take the interpretation that the model represents a good prediction of the mean scattering strength for such a bottom and for given interaction angles. Although we cannot form an ensemble average over the random scatterers while holding all angles fixed, the omni time series represents a kind of ergodic ensemble average over a distribution of interaction angles. If we take that data/model comparison as a measure of the model's fidelity, then calculations from the model for interaction angles that were sampled by the acoustic data serve as our estimate of scattering strength inferred from the measurements.

We proceed to present a few of the characteristics of bistatic scattering from basalt. There are many ways to display a function of three variables. To emphasize the bistatic effects

we show the bistatic scattering strength as a function of bistatic angle for fixed source and receiver grazing angles. Figs. 10-13 show the results for equal source and receiver grazing angles of 10°, 20°, 40°, and 70°. For comparison Lambert's law with the MacKenzie coefficient (-27 dB) is given by the dashed line. As expected when large time spread is observed, there is also large angular spread and high scattering strength levels. Secondly, we notice that the decay with bistatic angle increases at lower grazing angles and is very significant. We also notice again the remnants of the basalt reflectivity curve. The compressional and shear critical angles are most noticeable here in the 20° and 40° grazing-angle curves.

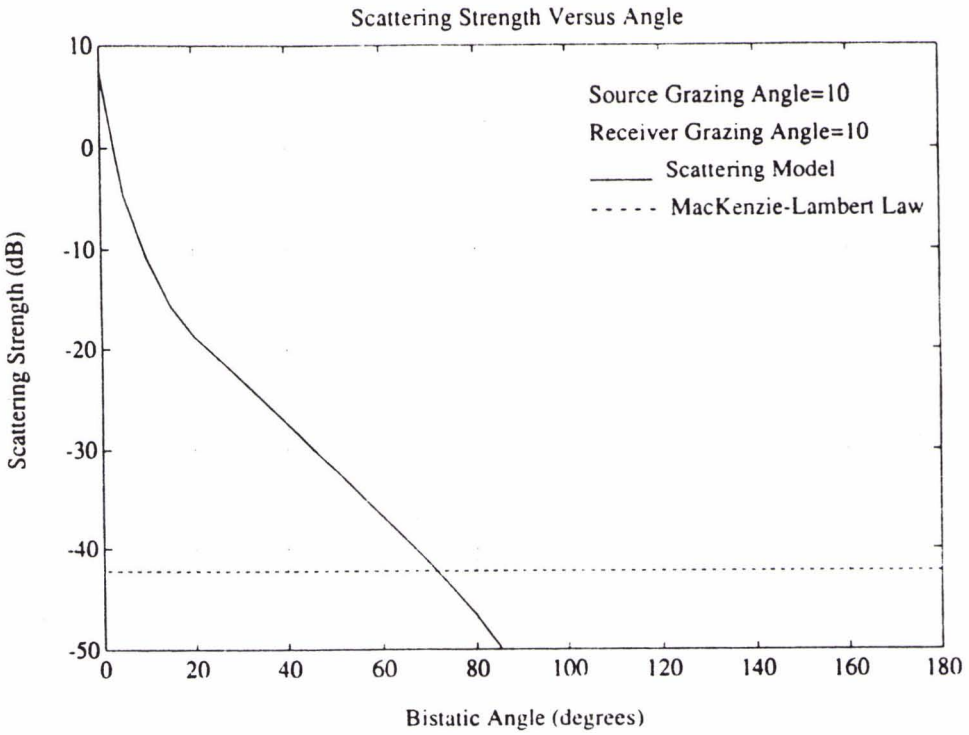

Fig. 10. Scattering strength versus bistatic angle; source and receiver grazing angles are 10°.

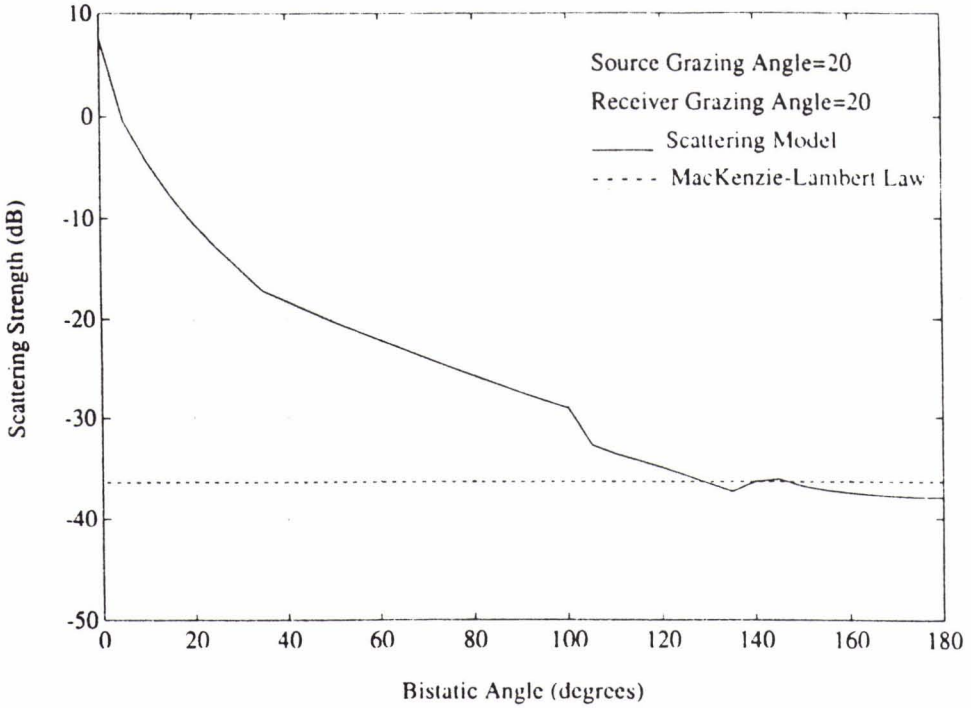

Fig. 11. Scattering strength versus bistatic angle; source and receiver grazing angles are 20°.

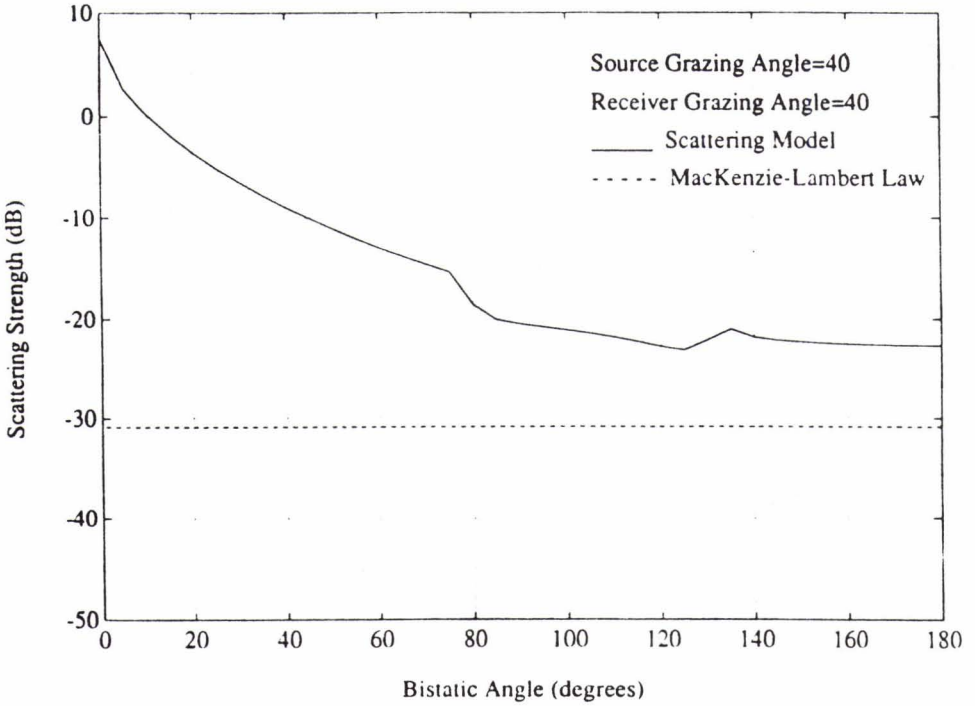

Fig. 12. Scattering strength versus bistatic angle; source and receiver grazing angles are 40°.

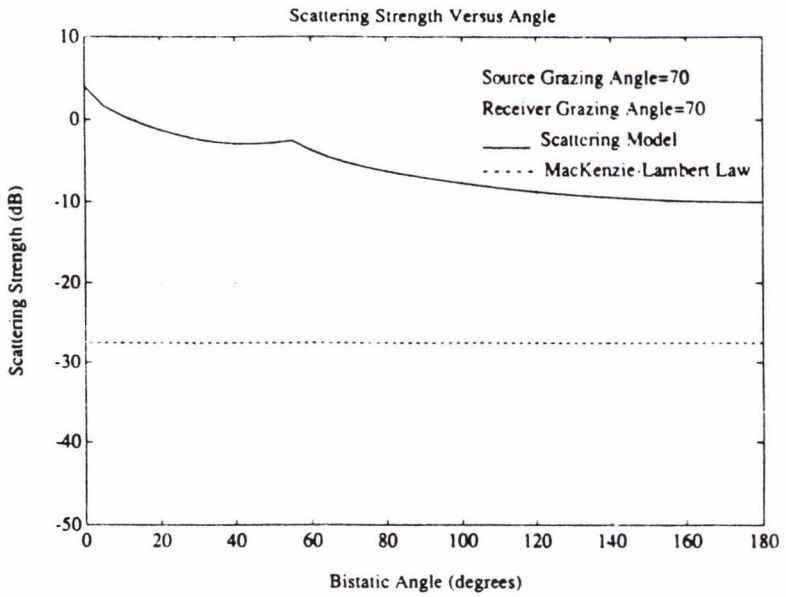

Fig. 13. Scattering strength versus bistatic angle; source and receiver grazing angles are 70°.

5. Summary And Conclusions

Bottom reflected signals were measured at an abyssal hills site in the Northeast Pacific using SUS charges as a source. The time series received on an omni-directional hydrophone exhibited large time spreads typical of those thin sediment sites. Although the time spread at the -20 dB level was large (~1 sec) a sharp peak occurred at signal onset.

Theoretical time series were calculated using Kirchhoff theory in the high-frequency limit together with a slope density function taken from Deep Tow measurements at the East Pacific Rise. The theory was in good agreement with the data, accounting for the early narrow peaks as well as for the very slow fall-off at later times. At 79.5° agreement was good over the 6.5 seconds duration of the first bottom bounce (before onset of the second bottom bounce) representing almost 30 dB of dynamic range.

The combination of basalt reflectivity and slope density controlled scattering strength gave correct levels without resort to adjustable parameters. The time-spread function convolved with (target-reflected) signals causes loss of signal energy that increases with bandwidth of the system.

The acoustic data was collected about 2000 km from the East Pacific Rise Crest, where data for the slope density function was collected. This suggests that basalt roughness changes very little over the geologic time that the crust moves from the spreading center where it was formed, westward to the present location where the acoustic data was taken.

Theoretical predictions were also made for a Gaussian slope density function and a function based on high resolution Seabeam data. The Gaussian slope density calculation failed dramatically at long delays relative to the first arrival. This fact demonstrates the importance of the non-Gaussian nature of bottom roughness. The Seabeam density calculation did little better. Lateral resolution for Seabeam at this depth (5 km water depth) and Deep Tow are on the order of 300m and 5m, respectively. The highest frequency in the acoustic data (300 Hz) has a wavelength of 5m. This suggests that bathymetric data must be acquired with spatial sampling about as fine as the acoustic wavelength in order to give meaningful basement slopes.

Beam time series for the narrow array beam were also predicted in the mean by the model. Calculations of bistatic scattering strength based on the model gave values higher than Lambert's law in most instances and exhibited a strong dependence on bistatic angle.

Acknowledgments: This work was sponsored by the ASW Environmental Acoustic Support (AEAS) Detachment of the Office of Naval Research (ONR) under the program direction of Edward Estalote. I would like to thank Michael Brill for reviewing this paper. Parts of his computer code for the broken mirror model were used directly in this model. He also engaged the author in many enlightening discussions. Dalcio Dacol very kindly supplied the computer code for calculation of the reflection coefficient for an elastic half space. Peter Lonsdale and Jim Smith provided the Seabeam data. Thanks are extended to Chuck Spofford and Paul Stokes for their encouragement and for many useful technical discussions. Data for this paper was collected under AEAS and ONR sponsorship during Pacific Echo II by the Naval Research Laboratory and the Defence Research Establishment Pacific. I wish to thank Orest Diachok for overall program guidance throughout the series of experiments. The cooperation and assistance of Ross Chapman as the Canadian Chief Scientist was invaluable in achieving both mutual and dissimilar goals. Finally, I would like to thank the many participants of both the US and Canadian teams that made the experiment a success.

References

[1]. McCammon, D. F., "A sediment time--angle spreading model," J. Acoust. Soc. Am. 87, 1126-1133 (1990).
[2]. Larson, R. L., and Spiess, F. N., "Slope distributions of the East Pacific Rise Crest," SIO Ref. 70-8, Marine Physical Laboratory of the Scripps Institution of Oceanography, San Diego, California 92152, 1970.
[3]. Spiess, F. N., Luyendyk, B. P., and Loughridge, M. S., "Bottom slope distributions an implied acoustic bearing errors in abyssal hill regions of the North Pacific," unpublished report, Office of Naval Research, Code 468 (April 1969).
[4]. Bass, F. G., and Fuks, I. M., *Wave Scattering From Statistically Rough Surfaces*, (Pergamon Press Ltd., Oxford, England, 1979).
[5]. Papoulis, A., *Probability, Random Variables, And Stochastic Processes*, Second Edition (McGraw-Hill Book Company, New York, 1984).
[6]. Bracewell, R. N., *The Fourier Transform and Its Applications*, (McGraw-Hill, Inc., New York, 1986).